## Three- $\alpha$ configurations of the second $J^{\pi} = 2^+$ state in ${}^{12}C$

H. Moriya<sup>1</sup> <sup>a</sup>, W. Horiuchi<sup>2,3,4,1</sup> <sup>b</sup>, J. Casal<sup>5</sup>, and L. Fortunato<sup>6,7</sup>

<sup>1</sup> Department of Physics, Hokkaido University, Sapporo 060-0810, Japan

<sup>2</sup> Department of Physics, Osaka Metropolitan University, Osaka, 558-8585, Japan

- <sup>3</sup> Nambu Yoichiro Institute of Theoretical and Experimental Physics (NITEP), Osaka Metropolitan University, Osaka 558-8585, Japan
- <sup>4</sup> RIKEN Nishina Center, Wako 351-0198, Japan
- <sup>5</sup> Departamento de Física Atómica, Molecular y Nuclear, Facultad de Física, Universidad de Sevilla, Apartado 1065, E-41080 Sevilla, Spain
- <sup>6</sup> Dipartimento di Fisica e Astronomia "G.Galilei", Universit degli Studi di Padova, via Marzolo 8, Padova I-35131, Italy

<sup>7</sup> INFN-Sezione di Padova, via Marzolo 8, Padova I-35131, Italy

Received: date / Revised version: date

Abstract. We investigate geometric configurations of  $\alpha$  (<sup>4</sup>He nucleus) clusters in the second  $J^{\pi} = 2^+$  state of <sup>12</sup>C, which has been discussed as a rotational band member of the second 0<sup>+</sup> state, the Hoyle state. The ground and excited 0<sup>+</sup> and 2<sup>+</sup> states are described by a three- $\alpha$  cluster model. The three-body Schrödinger equation with orthogonality conditions is accurately solved by the stochastic variational method with correlated Gaussian basis functions. To analyse the structure of these resonant states in a convenient form, we introduce a confining potential. The two-body density distributions together with the spectroscopic information clarify the structure of these states. We find that main configurations of both the second 0<sup>+</sup> and 2<sup>+</sup> states are acute-angled triangle shapes originating from the <sup>8</sup>Be(0<sup>+</sup>)+ $\alpha$  configuration. However, the <sup>8</sup>Be +  $\alpha$  components in the second 2<sup>+</sup> state become approximately 2/3 because the <sup>8</sup>Be subsystem is hard to excite, indicating that the state is not an ideal rigid rotational band member of the Hoyle state.

## 1 Introduction

An  $\alpha$  (<sup>4</sup>He nucleus) cluster is one of the most fundamental ingredients for understanding the structure of nuclei. The first excited  $J^{\pi} = 0^+$  state of <sup>12</sup>C, the so-called Hoyle state, is believed to play a crucial role in generating the  $^{12}$ C element in the universe [1]. For more than half a century, the Hoyle state has been studied by various theoretical models. As the state has a significant amount of the  ${}^{8}\text{Be}(0^{+}) + \alpha$  configurations [2,3,4,5,6], the Hoyle state decaves dominantly via sequential decay process  ${}^{8}\text{Be}(0^{+})\alpha \rightarrow$  $3\alpha$  [7]. On the other hand, Ref. [8] claimed that the Hoyle state has the  $\alpha$ -condensate-like character, where three  $\alpha$ bosons occupy the same S orbit. The structure of the Hoyle state has also been discussed in terms of geometric configurations of three- $\alpha$  particles based on the algebraic cluster model (ACM) [9,10,11]. Fully microscopic calculations predicted a significant amount of  $\alpha$  cluster configurations in the Hoyle state [12,13]. Prominent three- $\alpha$ cluster structure configurations were confirmed in density functional theory [14,15] and very recently in the Monte Carlo Shell Model approach [16] The evidence of the three $\alpha$  cluster structure can also be seen in its density profile of the ground state [17].

The search for other excited cluster states with some analogy to the Hoyle states has attracted interest. The structure of the second  $J^{\pi} = 2^+$  state is controversial as it can be a candidate of a rotational excited state of the Hoyle state forming the "Hoyle band" [18]. Experimentally, the existence of the  $2^+_2$  state was confirmed [19,20, 21,22 at 2.59(6) MeV above the three- $\alpha$  threshold with the decay width of 1.01(15) MeV [23]. The idea of the Hoyle band has attracted attention. Ref. [24] deduced a limit for the direct decay branching ratio of the Hoyle state under the assumption that the intrinsic structure of  $0^+_2$  and  $2^+_2$ are the same. Theoretically, the  $2^+_2$  state has only been recognized as having dominant  ${}^{8}\text{Be}(\bar{0}^{+}) + \alpha$  configurations, in which its intrinsic structure is a weakly-coupled <sup>8</sup>Be plus an  $\alpha$  particle with the angular momentum of 2 [4,5,6,13]. In analogy to the Hoyle state, the  $\alpha$ -mean field character in the  $2^+_2$  state can be considered, in which one  $\alpha$  particle is excited to the D orbit [25, 26] but Ref. [27] argued that the  $2^+_2$  state is not a simple rigid rotational excited state based on the analysis of the energy levels obtained by the microscopic three- $\alpha$  cluster model. In the context of the ACM, the  $2^+_2$  state is interpreted as the rigid rotational excited state of the Hoyle state in which three  $\alpha$  parti-

<sup>&</sup>lt;sup>a</sup> *e-mail:* moriya@nucl.sci.hokudai.ac.jp

<sup>&</sup>lt;sup>b</sup> *e-mail:* whoriuchi@omu.ac.jp

cles geometrically form an equilateral triangle and vibrate with the  $\mathcal{D}_{3h}$  symmetry [28]. To confirm whether this state belongs to the Hoyle state, a certain degree of similarity in the intrinsic structure should be observed. This motivates us to conduct a detailed study to clarify the extent of similarity between the structure of the second  $0^+$  and  $2^+$  states.

To settle this argument, in this paper, we study geometric configurations of three- $\alpha$  particles in the second 2<sup>+</sup> state and compare its structure with the second 0<sup>+</sup> Hoyle state using accurate three- $\alpha$  wave functions. <sup>8</sup>Be +  $\alpha$  components are analysed to clarify the origin of these configurations.

In this paper, the four physical states,  $J^{\pi} = 0_1^+, 0_2^+, 2_1^+$  and  $2_2^+$  of <sup>12</sup>C are studied within the three- $\alpha$  cluster model. In the next section, we explain our approach. Fully converged solutions are obtained by correlated Gaussian expansion with the stochastic variational method. They are briefly explained in Secs. 2.1 and 2.2. Geometric configurations of the  $\alpha$  particles are visualized by calculating two-body density distributions as well as other physical quantities. To evaluate these physical quantities of the state with rather a wide decay width such as the second  $2^+$  state, we introduce a confining potential. The details are given in Sec. 2.3. In Sec. 3, we show the numerical results and analysis. Finally, we draw a conclusion about the structure of the  $2^+_2$  state in Sec. 4.

## 2 Method

### 2.1 Three- $\alpha$ cluster model

In this paper, the wave functions of  $^{12}{\rm C}$  are described as a three- $\alpha$  system. The three- $\alpha$  Hamiltonian reads

$$H = \sum_{i=1}^{3} T_i - T_{\rm cm} + \sum_{i>j=1}^{3} (V_{2\alpha}^{ij} + V_{\rm Coul.}^{ij}) + V_{3\alpha}, \quad (1)$$

where  $T_i$  is the kinetic energy of the *i*th  $\alpha$  particle. The kinetic energy of the center-of-mass motion  $T_{\rm cm}$  is subtracted. The mass parameter in the kinetic energy terms and the elementary charge in the Coulomb potential ( $V_{\rm Coul.}$ ) are taken as  $\hbar^2/m_{\alpha} = 10.654$  MeVfm<sup>2</sup> and  $e^2 = 1.440$  MeVfm, respectively. Two- $\alpha$  interaction  $V_{2\alpha}$  is taken as the same used in Ref. [29], which is derived by a folding procedure using an effective nucleon-nucleon interaction. We employ the three- $\alpha$  interaction  $V_{3\alpha}$  depending on the total angular momentum  $J^{\pi}$  reproducing the energies of the  $0_1^+$  and  $2_1^+$  states as was used in Ref. [30]. Here we adopt the orthogonality condition model [31,32,33]. To impose the orthogonality condition to the Pauli forbidden states (f.s.), we introduce in the Hamiltonian the following pseudopotential [34]:

$$V_{\rm P} = \gamma \sum_{i>j=1}^{3} \sum_{nlm \in \rm f.s.} |\phi_{nlm}(ij)\rangle \langle \phi_{nlm}(ij)|.$$
(2)

The summation of nlm runs over all the f.s., i.e., 0S, 1S, and 0D states. We adopt the harmonic oscillator wave functions for  $\phi_{nlm}$  with the size parameter  $\nu = 0.2575$ fm<sup>-2</sup> [29] reproducing the size of the  $\alpha$  particle. Taking  $\gamma$ large enough, we exclude the Pauli forbidden states variationally from numerical calculations. In this paper, we take  $\gamma = 10^5$  MeV. The f.s. components of the resulting wave functions are found to be in the order of  $10^{-5}$ .

#### 2.2 Correlated Gaussian expansion

Denoting the *i*th single  $\alpha$  particle coordinate vector by  $\mathbf{r}_i$  (i = 1, 2, 3), we define a set of Jacobi coordinates  $\mathbf{x}_1 = \mathbf{r}_2 - \mathbf{r}_1$  and  $\mathbf{x}_2 = \mathbf{r}_3 - (\mathbf{r}_1 + \mathbf{r}_2)/2$ , excluding the center-of-mass coordinate  $\mathbf{x}_3 = (\mathbf{r}_1 + \mathbf{r}_2 + \mathbf{r}_3)/3$ , which are denoted as  $\tilde{\mathbf{x}} = (\mathbf{x}_1, \mathbf{x}_2)$ , where a tilde stands for the transpose of a matrix. The *k*th state of the three- $\alpha$  wave function  $\Psi_{JM}^{(k)}(\mathbf{x})$  with the total angular momentum *J* and its projection *M* is expressed in a superposition of fully symmetrized correlated Gaussian basis functions *G* [35, 36],

$$\Psi_{JM}^{(k)} = \sum_{i=1}^{K} C_i^{(k)} G(A_i, u_i, \boldsymbol{x}), \qquad (3)$$

$$G(A_i, u_i, \boldsymbol{x}) = \mathcal{S} \exp\left(-\frac{1}{2}\tilde{\boldsymbol{x}}A_i \boldsymbol{x}\right) \mathcal{Y}_{JM}(\tilde{u}_i \boldsymbol{x}), \quad (4)$$

where S is the symmetrizer which makes basis functions symmetrized under all particle-exchange, ensuring bosonic properties of  $\alpha$  particles. A variational parameter  $A_i$  is a 2 by 2 positive definite symmetric matrix, and  $\tilde{\boldsymbol{x}}A\boldsymbol{x}$  is a short-hand notation of  $\sum_{i,j=1}^{2} A_{ij}\boldsymbol{x}_i \cdot \boldsymbol{x}_j$ . The angular part of the wave function is described by using the global vector  $\tilde{\boldsymbol{u}}\boldsymbol{x} = \sum_{j=1}^{2} u_j \boldsymbol{x}_j$  with  $\tilde{\boldsymbol{u}} = (u_1, u_2)$  and  $u_2^2 = 1 - u_1^2$  [36,37]. A set of linear coefficients  $C_i^{(k)}$  is determined by solving the generalized eigenvalue problem,

$$\sum_{j=1}^{K} H_{ij} C_j^{(k)} = E^{(k)} \sum_{j=1}^{K} B_{ij} C_j^{(k)} \quad (i = 1, \dots, K), \quad (5)$$

where the matrix elements  $H_{ij}$  and  $B_{ij}$  are defined as

$$H_{ij} = \langle G(A_i, u_i, \boldsymbol{x}) | H | G(A_j, u_j, \boldsymbol{x}) \rangle \tag{6}$$

$$B_{ij} = \langle G(A_i, u_i, \boldsymbol{x}) | G(A_j, u_j, \boldsymbol{x}) \rangle.$$
(7)

The variational parameters  $A_i$  and  $u_i$  are determined by the stochastic variational method [35,36]. For more details of the optimization procedure, the reader is referred to Refs.[38,39].

#### 2.3 Confining potential

Ì

In this paper, we treat resonant  $0_2^+$  and  $2_2^+$  states as a bound state. This is the so-called bound-state approximation and works well for a state with a narrow decay width such as the  $0_2^+$  state (Expt.:  $\Gamma = 8.5 \times 10^{-3}$  MeV [40]), while for the  $2_2^+$  state it is hard to obtain the physical state with a simple basis expansion [41] as it has somewhat a large decay width (Expt.:  $\Gamma = 1.01(15)$  MeV [21]). To estimate the resonant energy, the analytical continuation in the coupling constant [42] is useful but does not provide us with the wave function. Nevertheless, a square-integrable wave function of a resonant state is useful to analyse its structure. A confining potential (CP) method [43,44] is suitable for this purpose, as we can treat a resonance state as a bound state inside of the CP. To get a physical resonant state in the bound-state approximation, we introduce the CP in the following parabolic form [43] as

$$V_{\rm CP} = \sum_{i=1}^{3} \lambda \Theta(|\boldsymbol{r}_i - \boldsymbol{x}_3| - R_0)(|\boldsymbol{r}_i - \boldsymbol{x}_3| - R_0)^2, \quad (8)$$

where  $\Theta(r)$  is the Heaviside step function,

$$\Theta(x) = \begin{cases} 1 & (x > 0) \\ 0 & (x < 0) \end{cases}.$$
 (9)

The strength  $\lambda$  and range  $R_0$  parameters of the CP are **Tak** real numbers and have to be taken appropriately. Here we three investigate the stability of the energies as well as the rootmean-square (rms) radii of  $\alpha$  particles  $R_{\rm rms} = \sqrt{\langle \Psi_{JM} | (\boldsymbol{r}_1 - \boldsymbol{x}_3)^2 \rangle}$ of the  $0^+_1, 0^+_2, 2^+_1$ , and  $2^+_2$  states against changes of  $\lambda$  and  $R_0$ .

Figure 1 shows the energies and rms radii of the  $0_1^+$ ,  $0_2^+, 2_1^+$  and  $2_2^+$  states with different  $R_0$ . The strength of the confining potential is set to be  $\lambda = 100 \text{ MeV/fm}^2$ . Since the  $R_0$  value is taken large enough, the energies and the rms radii of the bound states, the  $0_1^+$  and  $2_1^+$  states, do not depend much on these parameters. Even for the resonant  $0^+_2$  and  $2^+_2$  states, we find that the fluctuations of the energies are small about 0.1 MeV and 0.6 MeV, respectively, in the range of  $R_0 = 8-10$  fm. This is reasonable considering the facts that the  $0^+_2$  state has a quite small decay width and the  $2^+_2$  state has a larger decay width. The magnitude of the radius fluctuation against the changes of  $R_0$  is about  $\approx 0.3$  fm for the  $0^+_2$  state and  $\approx 0.5~{\rm fm}$  for the  $2^+_2$  state. We also made the same analysis by strengthening the strength  $\lambda$  by 10 times and a similar plot was obtained. Hereafter, we use the results with  $R_0 = 9 \text{ fm}, \lambda = 100 \text{ MeV/fm}^2.$ 

Table 1 lists the calculated energies and rms radii of  $\alpha$  particles. These energy values can be compared with the real parts of the complex energies obtained by the complex scaling method (CSM) [30]. The energies are 0.75 and 2.24 MeV for the  $0_2^+$  and  $2_2^+$  states, respectively, which are in good agreement with our results. Finally, we obtain the rms radii of the  $0_2^+$  and  $2_2^+$  states using these obtained wave functions. They are found to be similar and significantly large compared to the  $0_1^+$  and  $2_1^+$  states. For the sake of convenience, we also list the charge radii evaluated by  $R_{\rm ch} = \sqrt{r_{\alpha}^2 + R_{\rm rms}^2}$ , where  $r_{\alpha}$  is the charge radius of an  $\alpha$  particle, 1.6755(28) fm [45]. The calculated result for the ground state agrees with the theoretical result [46],

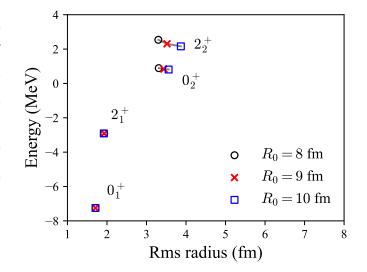


**Fig. 1.**  $R_0$  dependence in the CP. Energies and rms radii of the  $0_1^+$ ,  $0_2^+$ ,  $2_1^+$ , and  $2_2^+$  states with  $R_0 = 8,9$  and 10 fm are plotted. The strength of the confining potential  $\lambda$  is set to be 100 MeV/fm<sup>2</sup>. See text for details.

**Table 1.** Calculated energies measured from the three- $\alpha$  threshold, rms radii of  $\alpha$  particles, and charge radii

$\xrightarrow{2 \Psi_{JM}\rangle} \xrightarrow{\text{of the } 0^+_1, 0^+_2, 2^+_1, \text{ and } 2^+_2 \text{ states.}} J^{\pi} \xrightarrow{E} (\text{MeV}) \xrightarrow{R_{\text{rms}}} (\text{fm}) \xrightarrow{R_{\text{ch}}} R_{\text{ch}} (\text{fm})$										
$ \Psi JM$	$J^{\pi}$	$E \ (MeV)$	$R_{\rm rms}~({\rm fm})$	$R_{\rm ch}~({\rm fm})$						
	$0_{1}^{+}$	-7.25	1.71	2.39						
	$0^{+}_{2}$	0.84	3.44	3.83						
	$2_{1}^{+}$	-2.92	1.93	2.56						
	$2^{+}_{2}$	2.32	3.50	3.88						

showing reasonable reproduction of the measured chargeradius data 2.4702(22) fm [45]. A large charge radius of the  $0_2^+$  state is also consistent with that obtained in Ref. [46] though its radius was given as a complex number.

## **3** Results

### 3.1 Three- $\alpha$ configurations: Two-body density

To discuss the geometric configurations of the three- $\alpha$  systems, it is intuitive to see the two-body density distributions with respect to the two relative coordinates,  $x_1$  and  $x_2$ , defined by

$$\rho(r,R) = \langle \Psi | \delta(|\boldsymbol{x}_1| - r) \delta(|\boldsymbol{x}_2| - R) | \Psi \rangle, \qquad (10)$$

Note that the distribution is normalized as  $\int_0^\infty dr \int_0^\infty dR \rho(r, R) = 1$ . Figure 2 plots the two-body density distributions of the  $J^{\pi} = 0_1^+, 0_2^+, 2_1^+, \text{ and } 2_2^+$  states. For a guide to the eyes, the specific r/R ratios are indicated by the dashed lines and their corresponding geometric shapes are depicted by inset figures. We remark that the two-body density distributions were already discussed for the  $J^{\pi} = 0^+$  states in detail by using the shallow potential models [7,47]. Here

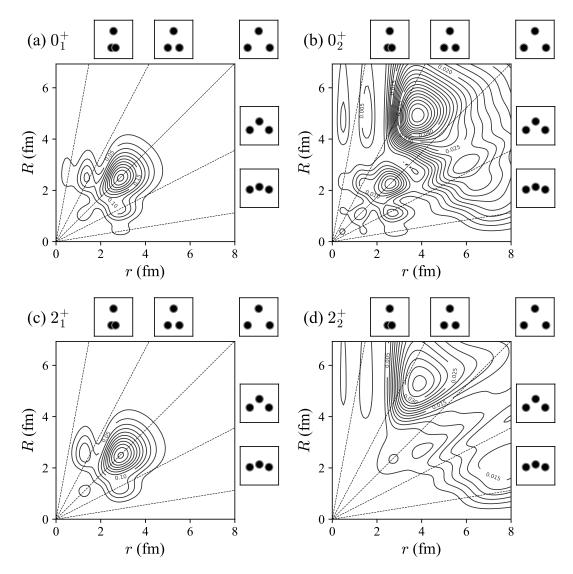


Fig. 2. Two-body density distributions  $\rho(r, R)$  of the (a)  $J^{\pi} = 0^+_1$ , (b)  $0^+_2$ , (c)  $2^+_1$ , and (d)  $2^+_2$  states. Contour intervals are 0.025 fm<sup>-2</sup> for  $0^+_1$  and  $2^+_1$  and 0.0025 fm<sup>-2</sup> for  $0^+_2$  and  $2^+_2$ . Specific r/R ratios are indicated by dashed lines and their geometric configurations are illustrated in small panels, e.g., the diagonal dashed line indicates the equilateral triangle configurations.

we present the results with the OCM. The preliminary results for the  $0^+$  states were already discussed in Ref. [48] but we repeat it to remind the characteristics of the twobody density distributions and to compare it with the  $2^+$  state.

The two-body density distributions of the  $0_1^+$  and  $2_1^+$  states have similar peak structures; the most dominant peak is located on the equilateral triangle configuration at  $r \sim 3$  fm and some other peaks come from the nodal behavior of wave function due to the orthogonality of the forbidden states. We see different fine structures when a shallow potential model is employed. See Ref. [48] for detailed comparison.

In contrast to the compact ground state, the two-body density distribution of the  $0_2^+$  state is widely spreading. The most dominant peak of the  $0_2^+$  state distribution is located at the acute-angled triangle configuration, which comes from the  ${}^{8}\text{Be}(0^{+}) + \alpha$  structure [48]. For the  $2^{+}_{2}$  state, likely to the  $0^{+}_{2}$  state, the two-body density distribution spreads and the most dominant peak is located at the acute-angled triangle configuration. However, we find that the amplitude is significantly smaller than the  $0^{+}_{2}$  state. The difference of these peak structures between the  $0^{+}_{2}$  and  $2^{+}_{2}$  states implies different intrinsic structure, which will be discussed in the next subsection.

At a closer look, we see the small peaks in the internal regions for the  $0^+_2$  state, while they disappear for the  $2^+_2$  state. This peak structure comes from the occupation of the nodal S orbit but the occupation number in the  $2^+_2$  state is much smaller than that of the  $0^+_2$  state [26]. Because the  $2^+_1$  state already has a large occupation number of the S orbit, there is no space to accommodate the nodal S orbit in the  $2^+_2$  state which should be orthogonal to the  $2^+_1$  state.

# 3.2 Partial-wave and $^8\text{Be}$ components in the three- $\alpha$ wave functions

In this subsection, we discuss more detailed structure of these three- $\alpha$  wave functions. For this purpose it is convenient to calculate the partial-wave component and <sup>8</sup>Be spectroscopic factor, which are respectively defined by

$$P_{l_1 l_2} = \frac{3!}{2! 1!} |\langle [Y_{l_1}(\hat{\boldsymbol{x}}_1) Y_{l_2}(\hat{\boldsymbol{x}}_2)]_{JM} | \Psi_{JM} \rangle |^2, \qquad (11)$$

$$S_{l_1 l_2} = \frac{3!}{2! 1!} |\langle \phi_{l_1}(x_1) [Y_{l_1}(\hat{x}_1) Y_{l_2}(\hat{x}_2)]_{JM} |\Psi_{JM}\rangle|^2, \quad (12)$$

where  $\phi_l$  is the radial wave functions of <sup>8</sup>Be with the relative angular momentum l = 0, 2, or 4, which correspond to physical resonant states with  $J^{\pi} = 0^+, 2^+$  or  $4^+$ , respectively, obtained by solving the two- $\alpha$  system using the same two- $\alpha$  potential adopted in this paper. The CP is also applied to evaluate these resonant states, and hence the obtained wave functions are square-integrable. The  $P_{l_1 l_2}$ value is the probability of finding  $(l_1, l_2)$  component in the three- $\alpha$  wave function, while the  $S_{l_1 l_2}$  value can be a measure of the the <sup>8</sup>Be +  $\alpha$  clustering. Note that given  $l_1$  and  $l_2$ ,  $S_{l_1 l_2}$  is a subspace of  $P_{l_1 l_2}$ , hence  $S_{l_1 l_2} \leq P_{l_1 l_2}$  always holds.

Table 2 lists the  $P_{l_1l_2}$  and  $S_{l_1l_2}$  values for the 0<sup>+</sup> and 2<sup>+</sup> states. The 0<sup>+</sup><sub>1</sub> state has almost equal  $P_{l_1l_2}$  values for  $l_1 = l_2 = 0, 2, \text{ and } 4$ , which can be explained by reminding that the state has the SU(3)-like character [26]. The higher partial-wave components is found to be  $\approx 1\%$ . The 0<sup>+</sup><sub>1</sub> wave function has about 50% of the <sup>8</sup>Be +  $\alpha$  component. The 2<sup>+</sup><sub>1</sub> state is mainly composed of  $(l_1, l_2) = (2, 2)$  and (4, 4) components,  $P_{22}$  and  $P_{44}$ , reflecting SU(3) character as like the 0<sup>+</sup><sub>1</sub> state [26] and also contains about half of the <sup>8</sup>Be +  $\alpha$  component. Consequently, the structure of the 2<sup>+</sup><sub>1</sub> state can be interpreted as a rigid rotational excited state of the 0<sup>+</sup><sub>1</sub> while keeping its geometric shape as was shown in Fig. 2.

On contrary, the  $P_{l_1l_2}$  values of  $0_2^+$  concentrate only on the  $l_1 = l_2 = 0$  channel about 80%, which is consistent with the microscopic cluster model calculations [49, 26]. This characteristic behavior is often interpreted as the bosonic condensate state of the three- $\alpha$  particles [8, 26]. This  $(l_1, l_2) = (0, 0)$  channel mostly consists of the <sup>8</sup>Be $(0^+) + \alpha$  component shown in Table 2, forming the acute-angled triangle shape in the two-body density distribution [48].

For the  $2_2^+$  state, dominant partial-wave components are the  $(l_1, l_2) = (0, 2)$  and (2, 0) channels. The <sup>8</sup>Be $(0^+) + \alpha$ component is dominant in the  $(l_1, l_2) = (0, 2)$  channel, while few <sup>8</sup>Be $(2^+) + \alpha$  component is found in the  $(l_1, l_2) =$ (2, 0) channel, which is in contrast to the  $0_2^+$  state mainly consisting of the <sup>8</sup>Be +  $\alpha$  configuration. This strong suppression can naturally be understood by considering the fact that the excitation energy of <sup>8</sup>Be $(2^+)$  is rather high 3.26 MeV (Expt.: 3.12 MeV [50]), compared to the calculated energy spacing between the  $0_2^+$  and  $2_2^+$  states,  $\approx 1.4$ MeV. This suggests that the  $2_2^+$  state is not a simple rigid rotational excited state of the  $0_2^+$  state but a partially rotational state. We remark that this interpretation supports the mean-field-like picture: The three  $\alpha$  particles occupy the same S state in the  $0^+_2$  state [8], while one S-state  $\alpha$ particle is excited to the D state in the  $2^+_2$  state [26]. Such a D-wave excitation is possible with lower energy than the <sup>8</sup>Be excitation if the frequency of the mean-field potential is low enough.

### 3.3 Spectroscopic amplitude

To discuss the role of the dominant channels in the geometric configurations in the  $0^+_2$  and  $2^+_2$  states, it is useful to evaluate the <sup>8</sup>Be spectroscopic amplitude (SA)

$$\theta_{l_1 l_2}(R) = \sqrt{\frac{3!}{2!1!}} \frac{1}{R} \\ \times \langle \phi_{l_1}(x_1) \left[ Y_{l_1}(\hat{\boldsymbol{x}}_1) Y_{l_2}(\hat{\boldsymbol{x}}_2) \right]_{JM} \delta(|\boldsymbol{x}_2| - R) |\Psi_{JM}\rangle.$$
(13)

Note that  $\int_0^\infty dR [R\theta_{l_1l_2}(R)]^2 = S_{l_1l_2}$ . For practical calculations, see Appendix A of Ref. [51], where an explicit formula of the SA with the correlated Gaussian basis function was given.

Figure 3 shows the SA with  $(l_1, l_2) = (0, 0)$  for the  $0_2^+$  state and (0, 2) for the  $2_2^+$  state, which respectively correspond to the dominant configurations for each state. The SA of the  $2_2^+$  state is smaller than that of the  $0_2^+$  state reflecting the magnitudes of the  $S_{l_1 l_2}$  values. For the sake of comparison, we also plot the radial wave function of <sup>8</sup>Be(0<sup>+</sup>),  $\phi_0(r)$ . The peak position of  $r\phi_0(r)$  is located at 3.68 fm, while the SA has the largest peak at 4.97 fm for the  $0_2^+$  state and 6.20 fm for the  $2_2^+$  state. Though the latter distribution is broad, these are consistent with the fact that the highest peak of the two-body density distribution is located at (r, R) = (3.9, 5.1) fm for the  $0_2^+$  state and (r, R) = (3.9, 5.3) fm for the  $2_2^+$  state, exhibiting the acute-angled triangle configuration as shown in Fig. 2. We also evaluate the rms radii of the SA defined by

 $D_{l_1l_2} = \sqrt{\int_0^\infty dR R^2 [R\theta_{l_1l_2}(R)]^2 / S_{l_1l_2}}$ , listed in Table 2. The SA radii of the dominant channel of the  $0_2^+$  and  $2_2^+$  states are 5.84 fm with  $(l_1, l_2) = (0, 0)$  and 7.38 fm with  $(l_1, l_2) = (0, 2)$ , respectively. Since the rms distance of the <sup>8</sup>Be wave function is 5.32 fm, the <sup>8</sup>Be +  $\alpha$  configuration induces an acute-angled triangle geometry.

## 4 Conclusion

How similar is the structure of the  $2^+_2$  state in the  ${}^{12}C$  as compared to the Hoyle state? We have made comprehensive investigations of the structure of  ${}^{12}C$  with a special emphasis on the geometric configurations of  $\alpha$  particles. The 0<sup>+</sup> and 2<sup>+</sup> states of  ${}^{12}C$  are described by a three- $\alpha$ cluster model with the orthogonality constraint. Precise three- $\alpha$  wave functions are obtained by using the correlated Gaussian expansion with the stochastic variational method. We introduce a confining potential to obtain a physical state, allowing us to visualize the three- $\alpha$  configuration by using square-integrable basis functions.

	$0_{1}^{+}$		$2_{1}^{+}$		$0_{2}^{+}$		$2_{2}^{+}$	
$(l_1l_2)$	$P_{l_1l_2}$	$S_{l_1l_2}$	$P_{l_1l_2}$	$S_{l_1 l_2}$	$P_{l_1l_2}$	$S_{l_1 l_2}$	$P_{l_1l_2}$	$S_{l_1 l_2}$
(00)	0.352	0.193	_	_	0.786	0.668	_	_
(02)	—	—	0.096	0.058	—	—	0.451	0.419
Subtotal $(l_1 = 0)$	0.352	0.193	0.096	0.058	0.786	0.668	0.451	0.419
(20)	-	-	0.095	0.054	-	_	0.374	0.021
(22)	0.351	0.175	0.483	0.268	0.112	0.027	0.044	0.011
(24)	-	-	0.006	0.003	-	-	0.020	0.007
Subtotal $(l_1 = 2)$	0.351	0.175	0.584	0.325	0.112	0.027	0.438	0.039
(42)	-	-	0.007	0.003	-	_	0.029	0.007
(44)	0.285	0.100	0.299	0.114	0.060	0.013	0.017	0.008
(46)	—	-	$\sim 10^{-4}$	$\sim 10^{-5}$	_	_	0.006	0.004
Subtotal $(l_1 = 4)$	0.285	0.100	0.306	0.117	0.060	0.013	0.052	0.019
Total	0.988	0.468	0.986	0.500	0.958	0.708	0.941	0.477

**Table 2.** Partial-wave component and <sup>8</sup>Be spectroscopic factor of the  $J^{\pi} = 0^+$  and  $2^+$  states. See text for details.

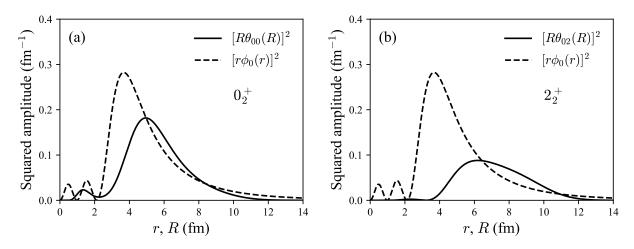


**Fig. 3.** Square of <sup>8</sup>Be spectroscopic amplitudes,  $[R\theta_{l_1l_2}(R)]^2$  with (a)  $(l_1, l_2) = (0, 0)$  and (b)  $(l_1, l_2) = (0, 2)$  for the  $0^+_2$  and  $2^+_2$  states. The square of the radial wave function of the <sup>8</sup>Be $(0^+)$  state  $[r\phi_0(r)]^2$  is also compared.

In comparison of the two-body density distributions of the  $0_2^+$  and  $2_2^+$  state, the main three- $\alpha$  configurations are found to be the same; the acute-angled triangle shape coming from the  ${}^{8}\text{Be}(0^{+}) + \alpha$  component. However, the magnitude is significantly smaller for the  $2^+_2$  state compared to the  $0^+_2$  state. We find that the  $2^+_2$  state can be mainly excited by the relative coordinate between <sup>8</sup>Be and  $\alpha$  consistently with the interpretation given in Refs [4,5, 6,13]. The <sup>8</sup>Be cluster in the  $0^+_2$  state is hardly excited because the excitation energy of the  ${}^{8}\text{Be}(2^{+})$  is higher than the energy difference of  $2^{+}_{2}$  state from the Hoyle state. Therefore, we conclude that the  $2^+_2$  state is not an ideal rigid Hoyle band but could be interpreted as a partially rotational excited state of  $0^+_2$ . We note, however, that this does not contradict the  $\alpha$ -particle mean-field picture for the  $2^+_2$  state [26]. It is interesting to study the  $4^+_2$  state, which is observed recently [18] and considered also as a candidate of the Hoyle band member.

This work was in part supported by JSPS KAKENHI Grants Nos. 18K03635 and 22H01214. We acknowledge the Collaborative Research Program 2022, Information Initiative Center, Hokkaido University.

## References

- 1. F. Hoyle, Astrophys. J. Suppl. Ser. 1, 12 (1954).
- 2. H. Horiuchi, Prog. Theor. Phys. **51**, 1226 (1974).
- 3. H. Horiuchi, Prog. Theor. Phys. **53**, 447 (1975).
- E. Uegaki, S. Okabe, Y. Abe, and H. Tanaka, Prog. Theor. Phys. 57, 1262 (1977).
- E. Uegaki, Y. Abe, S. Okabe, and H. Tanaka, Prog. Theor. Phys. 59, 1031 (1978).
- E. Uegaki, Y. Abe, S. Okabe, and H. Tanaka, Prog. Theor. Phys. 62, 1621 (1979).
- 7. S. Ishikawa, Phys. Rev. C **90**, 061604(R) (2014).
- 9. R. Bijker and F. Iachello, Ann. Phys. **298**, 334 (2004).
- 10. L. Fortunato, Phys. Rev. C 99, 031302(R) (2019).

- A. Vitturi, J. Casal, L. Fortunato, and E. G. Lanza, Phys. Rev. C 101, 014315 (2020).
- M. Chernykh, H. Feldmeier, T. Neff, P. von Neumann-Cosel, and A. Richter, Phys. Rev. Lett. 98, 032501 (2007).
- 13. Y. Kanada-En'yo, Prog. Theor. Phys.  ${\bf 117},\,655$  (2007).
- J.-P. Ebran, E. Khan, T. Nikšić, and D. Vretenar, Phys. Rev. C 87, 044307 (2013).
- J.-P. Ebran, M. Girod, E. Khan, R. D. Lasseri, and P. Schuck, Phys. Rev. C 102, 014305 (2020).
- T. Otsuka, T. Abe, T. Yoshida, Y. Tsunoda, N. Shimizu, N. Itagaki, Y. Utsuno, J. Vary, P. Maris, and H. Ueno, Nat. Commun. 13, 2234 (2022).
- W. Horiuchi and N. Itagaki, accepted for publication in Phys. Rev. C (Letter), in press, arXiv: 2301.05405.
- M. Freer, S. Almaraz-Calderon, A. Aprahamian, N. I. Ashwood, M. Barr, B. Bucher, P. Copp, M. Couder, N. Curtis, X. Fang, F. Jung, S. Lesher, W. Lu, J. D. Malcolm, A. Roberts, W. P. Tan, C. Wheldon, and V. A. Ziman, Phys. Rev. C 83, 034314 (2011).
- M. Itoh, H. Akimune, M. Fujiwara, U. Garg, H. Hashimoto, T. Kawabata, K. Kawase, S. Kishi, T. Murakami, K. Nakanishi, Y. Nakatsugawa, B.K. Nayak, S. Okumura, H. Sakaguchi, H. Takeda, S. Terashima, M. Uchida, Y. Yasuda, M. Yosoi, and J. Zenihiro, Nucl. Phys. A **738**, 268 (2004).
- M. Freer, H. Fujita, Z. Buthelezi, J. Carter, R. W. Fearick, S. V. Förtsch, R. Neveling, S. M. Perez, P. Papka, F. D. Smit, J. A. Swartz, and I. Usman, Phys. Rev. C 80, 041303(R) (2009).
- M. Itoh, H. Akimune, M. Fujiwara, U. Garg, N. Hashimoto, T. Kawabata, K. Kawase, S. Kishi, T. Murakami, K. Nakanishi, Y. Nakatsugawa, B. K. Nayak, S. Okumura, H. Sakaguchi, H. Takeda, S. Terashima, M. Uchida, Y. Yasuda, M. Yosoi, and J. Zenihiro, Phys. Rev. C 84, 054308 (2011).
- W. R. Zimmerman, M. W. Ahmed, B. Bromberger, S. C. Stave, A. Breskin, V. Dangendorf, Th. Delbar, M. Gai, S. S. Henshaw, J. M. Mueller, C. Sun, K. Tittelmeier, H. R. Weller, and Y. K. Wu, Phys. Rev. Lett. **110**, 152502 (2013).
- 23. J. H. Kelley, J. E. Purcell, and C. G. Sheu, Nucl. Phys. A 968, 71 (2017).
- 24. R. Smith, M. Gai, M. W. Ahmed, M. Freer, H. O. U. Fynbo, D. Schweitzer, and S. R. Stern, Phys. Rev. C 101, 021302(R) (2020).
- Y. Funaki, A. Tohsaki, H. Horiuchi, P. Schuck, and G. Röpke, Eur. Phys. J. A 24, 321 (2005).
- 26. T. Yamada and P. Schuck, Eur. Phys. J. A 26, 185 (2005).
- 27. Y. Funaki, Phys. Rev. C **92**, 021302(R) (2015).
- R. Bijker and F. Iachello, Prog. Part. Nucl. Phys. 110, 103735 (2020).
- K. Fukatsu and K. Katō, Prog. Theor. Phys. 87, 151 (1992).
- S. Ohtsubo, Y. Fukushima, M. Kamimura, and E. Hiyama, Prog. Theor. Exp. Phys. 2013, 073D02 (2013).
- 31. S. Saito, Prog. Theor. Phys. 40, 893 (1968).
- 32. S. Saito, Prog. Theor. Phys. 41, 705 (1969).
- 33. S. Saito, Prog. Theor. Phys. 62, 11 (1977).
- V. I. Kukulin, and V. N. Pomenertsev, Ann. Phys. (N. Y.) 111, 333 (1978).
- 35. K. Varga and Y. Suzuki, Phys. Rev. C 52, 2885 (1995).
- Y. Suzuki and K. Varga, Stochastic Variational Approach to Quantum-Mechanical Few-Body Problems, Lecture Notes in Physics (Springer, Berlin, 1998), Vol. m54.

- 37. Y. Suzuki, J. Usukura, and K. Varga, J. Phys. B: At. Mol. Opt. Phys. **31**, 31 (1998).
- Lai Hnin Phyu, H. Moriya, W. Horiuchi, K. Iida, K. Noda, and M. T. Yamashita, Prog. Theor. Exp. Phys. 2020, 093D01 (2020).
- 39. H. Moriya, H. Tajima, W. Horiuchi, K. Iida, and E. Nakano, Phys. Rev. C 104, 065801 (2021).
- 40. F. Ajzenberg-Selove, Nucl. Phys. A 506, 1 (1990).
- 41. Y. Funaki, H. Horiuchi, and A. Tohsaki, Prog. Theor. Phys. **115**, 115 (2006).
- V. I. Kukulin and V. M. Krasnopol'sky, J. Phys. A **10**, 33 (1977); V. I. Kukulin and V. M. Krasnopol'sky, M. Miselkhi, Sov. J. Nucl. Phys. **29**, 421 (1979).
- 43. J. Mitroy, J. Y. Zhang, and K. Varga, Phys. Rev. Lett. 101, 123201 (2008).
- J. Mitroy, S. Bubin, W. Horiuchi, Y. Suzuki, L. Adamowicz, W. Cencek, K. Szalewicz, J. Komasa, D. Blume, and K. Varga, Rev. Mod. Phys. 85, 693 (2013).
- I. Angeli and K. P. Marinova, At. Data Nucl. Data Tables 99, 69 (2013).
- 46. C. Kurokawa and K. Kato, Nucl. Phys. A 792, 87 (2007).
- 47. N. B. Nguyen, F. M. Nunes, and I. J. Thompson, Phys. Rev. C 87, 054615 (2013).
- H. Moriya, W. Horiuchi, J. Casal, and L. Fortunato, Few-Body Syst. 62, 46 (2021).
- H. Matsumura and Y. Suzuki, Nucl. Phys. A **739**, 238 (2004).
- 50. D. R. Tilley, J. H. Kelley, J. L. Godwin, D. J. Millener, J. E. Purcell, C. G. Sheu, and H. R. Weller, Nucl. Phys. A **745**, 155 (2004).
- Y. Suzuki, W. Horiuchi, K. Arai, Nucl. Phys. A 823, 1 (2009).